DOI: 10.15480/882.9347

Eighth International Symposium on Marine Propulsors
smp'24, Berlin, Germany, March 2024

Numerical Study on the Evolution of Vortex Structures at the Propeller Tip and Their Influence on Cavitation Inception

Stephan Berger [1,2], **Rasmus Møller Bering** [*1], **Max Steden** [1], **Keun Woo Shin** [1], **Jens Ring Nielsen** [1]

[1]MAN Energy Solutions, Hydrodynamics Research Department, Propeller & Aft Ship, Copenhagen/Frederikshavn, Denmark
[2]FORCE Technology, Hydro- and Aerodynamics, Kgs. Lyngby, Denmark

ABSTRACT

In this paper, we study the behaviour of propeller leading edge vortices, local tip vortices and trailing vortices for different operation conditions and tip geometries. It turns out that the pressure drop in the trailing vortex being relevant for cavitation inception strongly depends on the nature of the local tip vortex and of the leading edge vortex. Further, we demonstrate that applying tip rake to a given propeller design is an effective instrument to steer the vorticity distribution in the tip region allowing to increase cavitation inception speed while maintaining the propeller's efficiency. Open water simulations were carried out using a RANS method and the k-ω SST turbulence closure model with curvature correction. The computational mesh was appropriately refined along the leading edge, the propeller tip and along the axis of the trailing vortex. An intuitive method for evaluating vortex quantities such as circulation, viscous core radius, the level of vorticity and pressure drop at different stations along the vortex axis is presented and applied. Finally, our findings are underpinned by experimental results from a cavitation inception test.

Keywords
Propeller leading edge vortex, propeller tip vortex cavitation inception, vortex detection and analysis, design of silent propellers

1 INTRODUCTION

For ships with strict noise requirements, such as research vessels, fishery vessels, cruise vessels operating in sensitive areas as well as naval vessels, cavitation inception speed is a crucial design aspect. Under full-scale conditions, the onset of cavitation happens most likely in the tip region of the propeller, where distinct vortex structures formed during operation give rise to low pressures.

Classical and well-established design strategies for delaying cavitation inception involve a reduction of the blade load at the propeller tip and come with unavoidable losses in efficiency. Typically, the designer will add some safety margins against cavitation inception. In order to avoid unnecessary efficiency losses, efforts are made to keep these margins as low as possible. It is therefore of great interest to better understand the behaviour and control of vortex structures at the propeller tip.

For most modern propeller designs with skewed blades, depending on the operation condition, three distinguishable vortical structures occur in the blade tip region: (i) the leading edge vortex (LEV) originating from a local flow detachment at the propeller's leading edge, (ii) the local tip vortex (LTV) at the blade tip and (iii) the trailing vortex (TRV) absorbing vorticity shed from the trailing edge of the blade (Kuiper 2001).

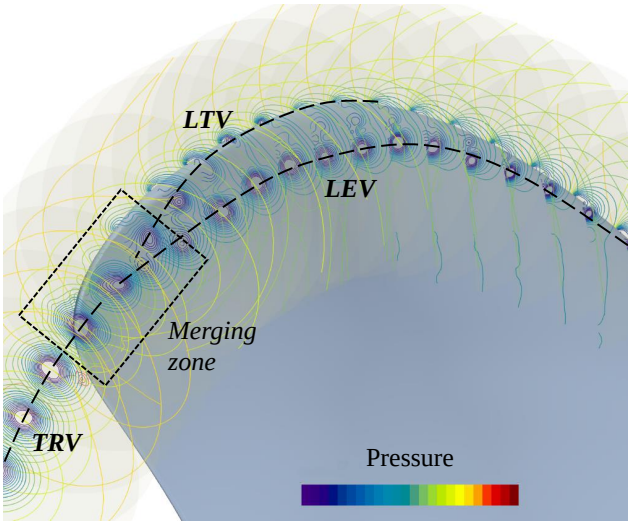

Figure 1: Leading edge vortex (LEV), local tip vortex (LTV) and trailing vortex (TRV) at the tip of a propeller blade. Pressure contour lines at different extraction planes.

Only very rarely, isolated trailing vortices can be observed within propeller flow. In most cases, it is either the "continuation" of the leading edge or local tip vortex, or – if both exist – a merging process takes place, where leading edge vortex and local tip vortex merge into the trailing vortex. It will be shown later that these different ways of formation have an influence on the structure of the trailing vortex close to the propeller tip and thus play an important role for cavitation inception.

Vortical flow related to marine hydrodynamics has been addressed by many authors. Only a few recent representative examples of the vast body of literature can be cited here. Various viscous simulations methods and the related challenges in the computation of vortex flows are addressed, for example, by Paskin et al. (2019), Feder (2021) or Asnaghi et al. (2019). Further insights are given by Krüger (2017) or Asnaghi et al. (2021), who investigate the influence of blade surface roughness on the structure of the trailing vortex aiming for delayed vortex cavitation inception. Reynolds number scale effects are numerically investigated by Park et al. (2021), who use a simple hydrofoil configuration in their work. Amini et al. (2019) experimentally study the influence of different wing tip configurations on trailing vortex cavitation inception for a hydrofoil. In particular, they evaluate the velocity field of the trailing vortex downstream of the foil.

Leading edge vortices play a vital role in lift generation at low Reynolds numbers. Hence, it is no surprise that extensive research is devoted to this flow phenomenon in the field of biology-inspired engineering, where the principles of insect flight are applied to, among others, small aircraft. For example, Widmann and Tropea (2015), Li et al. (2020) and Kissing et al. (2020) investigate formation and detachment of a leading edge vortex for unsteady flow over a flat plate. Even though, their work cannot directly be related to the scope of the present study, it provides a detailed description of the basic flow features of leading edge vortices. While still in the regime of small Reynolds numbers, Wojcik and Buchholz (2014) point out the fundamental differences between the aforementioned plate configuration and the formation of a leading edge vortex on a rotating blade. A comprehensive review has recently been published by Eldredge and Jones (2019).

A few publications have indeed a detailed look at the vortex structures at the propeller blade (Brown et al. 2015; Asnaghi et al. 2018, e.g.), however, a systematic study addressing the impact of leading edge and local tip vortex on the formation and structure of the trailing vortex is not known to the authors. The present study intents to close this gap by addressing the following aspects:

- How is the structure of the trailing vortex affected by the local tip vortex and – if present – by the leading edge vortex?
- How do blade tip shape and the operation condition affect the vortical structures at the propeller tip and, in particular, the onset of cavitation?

To investigate these aspects, a numerical study was conducted, involving a systematic variation of operation conditions and design parameters – tip unloading and tip rake – for a given, representative propeller design. The behaviour of the vortex structures was carefully examined using high-resolution viscous simulations with Simcenter *Star-CCM+*.

For the analysis of the results, pressure distributions and vorticity distributions were evaluated in several cross sections of the particular vortices at different stations along the blade leading edge, the blade tip, and downstream of the propeller tip. An intuitive method for vortex detection was applied together with a vortex analysis procedure providing main vortex characteristics such as circulation, the level of vorticity, viscous core radius, wall distance and pressure drop in the vortex core.

The paper is organised as follows: in Section 2, the numerical method and the meshing strategy as well as the techniques for vortex analysis are described. Section 3 comments on typical flow features encountered during the study, whereas in Section 4, the influence of blade tip geometry and operation condition is shown. Finally, in Section 5, a practical example is used to demonstrate the relevance of the observations made before. Here, we make use of experimental data in order to underpin our findings. The paper closes with a conclusion and recommendations for future work.

2 METHODOLOGY

In order to obtain a large variety of different flow patterns, the tip geometry of a given baseline propeller design was modified in a systematic manner. For that purpose, Friendship Systems *CAESES* was employed, whereas the viscous flow simulations were carried out using Simcenter *Star-CCM+*. Sections 2.1 and 2.2 provide details about the numerical method as well as the geometry generation and meshing strategy.

Viscous flow simulations provide detailed information about the three-dimensional flow field. These results were post-processed and brought to a problem-adapted form, where coherent vortical structures are identified and evaluated. The respective procedures are described in Sections 2.3 and 2.4. Section 2.5 provides an overview of the geometry variation and propeller variants as well as operation conditions investigated during the study.

2.1 Numerical Method

Robustness and efficiency were key requirements when selecting a suitable viscous simulation method for our study. Therefore, Simcenter *Star-CCM+* 2206 (NN 2022) was employed using the well-established RANS approach and the Menter k-ω SST turbulence closure model (Menter 1994) with flow curvature correction. Laminar–turbulent transition was modelled by using the γ-Re transition model (Langtry and Menter 2009). Convection terms were discretised using a second order-scheme.

Since the flow mechanisms leading to cavitation inception are of interest and not the behaviour of cavitation itself, the simulations were done without modelling cavitation.

Open water simulations were made in a cylindrical fluid domain with an inner cylindrical subdomain defined around the propeller. To reduce the computational effort, only one blade was considered; the effect of the other blades was considered by applying a symmetry boundary condition. Propeller rotation was modelled inside the subdomain using the moving reference frame (MRF) method.

The remaining boundary conditions were set as follows: a fixed velocity boundary condition was specified at the inlet boundary, whereas a pressure outlet boundary was prescribed at the outlet boundary; the outer cylinder shell was modelled as slip wall. The boundaries on the propeller blade surface (including hub and shaft) were specified as no-slip wall. Between the outer static domain and the inner rotational subdomain, an interface was set up in order to transfer flow field information between the two domains.

2.2 Geometry Generation and Meshing Strategy

All propeller geometries were generated using Friendship Systems *CAESES*. Here, a parametric model with in-house distribution functions for pitch, chord length, thickness, skew and rake was set up allowing for systematic variation of the propeller tip geometry. A small trailing edge radius was added to the profiles and the propeller tip was cut at $r/R = 0.995$ to achieve a more robust geometry and mesh generation.

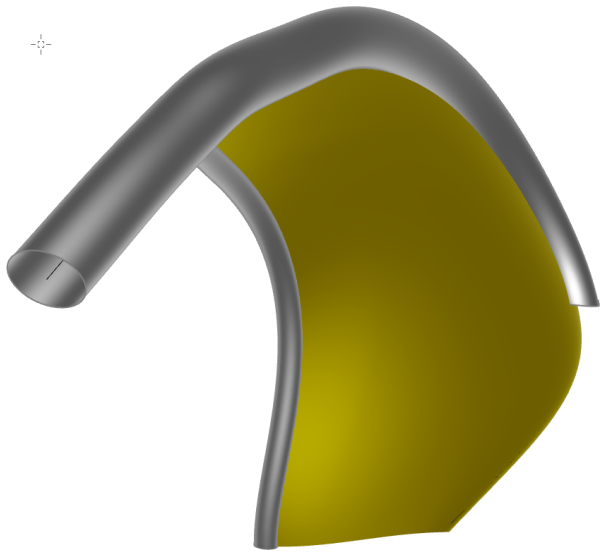

Figure 2: Refinement zones along leading edge, trailing edge, propeller tip and axis of the trailing vortex generated by *CAESES*.

In order to resolve relevant flow details, a refinement zone along leading edge, propeller tip and the trajectory of the trailing vortex was established as shown in Fig. 2. Another, but smaller refinement zone was defined around the trailing edge.

Since the trailing vortex trajectory is initially unknown, a low-resolution simulation was performed in advance in order to determine the trajectory. Adaptive grid refinement was not applied in order to maintain control over the refinement and ensure comparability between different simulations.

The computational domain was discretised using a trimmed hexahedral mesh with prism layers on the no-slip wall boundaries. 20 prism layers were used with a stretch factor of 1.1, where the height of the layer was specified to target $Y^+ < 1.0$. The all-Y^+ wall treatment was used to further increase robustness of the simulations.

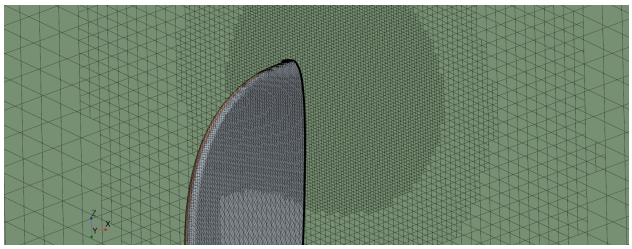

(a) Mesh refinement, vortex cross section.

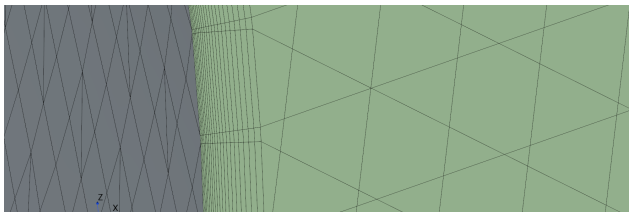

(b) Prism layers, blade surface.

Figure 3: Mesh details at the blade tip for mesh configuration M1cc (see Table 3).

2.3 Non-dimensional flow quantities

Throughout the entire paper, dimensional flow quantities $()'$ are made dimensionless by characteristic length and velocity scales. In particular, lengths and positions are made dimensionless by the propeller diameter D:

$$\mathbf{x} = (x, y, z) = \frac{1}{D}\left(x', y', z'\right), \tag{1}$$

with (x', y', z') being the dimensional position vector in global Cartesian coordinates. For velocities, nD is used with n being the number of revolutions:

$$\mathbf{v} = (v_x, v_y, v_z) = \frac{1}{nD}\left(v_x', v_y', v_z'\right). \tag{2}$$

This leads directly to the following expression for the dimensionless vorticity $\boldsymbol{\omega} = \nabla \times \mathbf{v}$:

$$\boldsymbol{\omega} = (\omega_x, \omega_y, \omega_z) = \frac{1}{n}\left(\omega_x', \omega_y', \omega_z'\right). \tag{3}$$

Pressure is expressed in terms of the pressure coefficient c_p:

$$c_p = \frac{p - p_{\text{ref}}}{1/2 \rho n^2 D^2} \tag{4}$$

with ρ being the density of water.

Further, integral forces acting on the blades are expressed in form of thrust coefficient $k_T = T\rho^{-1}n^{-2}D^{-4}$ and torque coefficient $k_Q = Q\rho^{-1}n^{-2}D^{-5}$, with T and Q being the dimensional propeller thrust and torque, respectively. With the advance velocity V and the advance coefficient $J = V/nD$, one obtains the open water efficiency $\eta = J/2\pi K_T/K_Q$.

In addition, the non-dimensional radial distribution of thrust $k_{T,r}$ is introduced:

$$k_{T,r}(r) = \frac{\mathrm{d}T}{\rho n^2 \mathrm{d}r D^3}, \tag{5}$$

with $\mathrm{d}T(r)$ being the thrust acting on a small radial stripe $\mathrm{d}r(r)$ of the blade surface.

2.4 Vortex analysis

For the analysis of vortex characteristics such as vortex circulation Γ, viscous core radius r_a and pressure drop $c_{p,\min}$, flow field data was extracted for a number of circular extraction planes S_i along the leading edge, the blade tip and the axis of the trailing vortex as shown in Fig. 4. For each plane, flow information consists of a large number of data points distributed in an unstructured manner. In the present section, the underlying concept of the data processing routines is described.

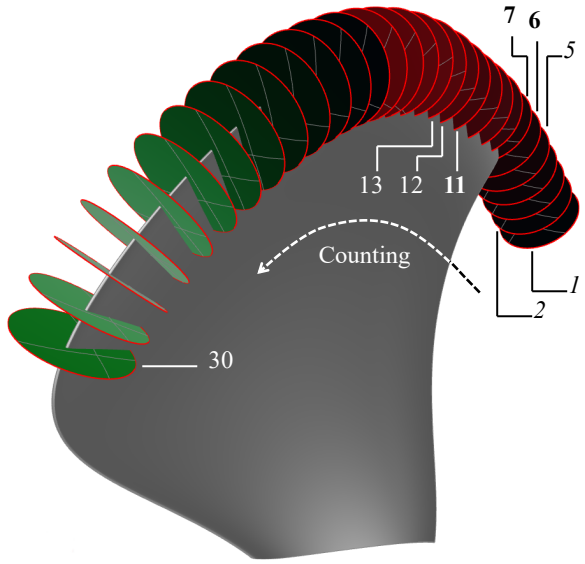

Figure 4: Extraction planes along the leading edge (planes 30 to 12), the propeller tip (**11** to **6**) and the axis of the trailing vortex (*5* to *1*) generated by *CAESES*. Numbering starts at the plane farthest downstream from the propeller tip.

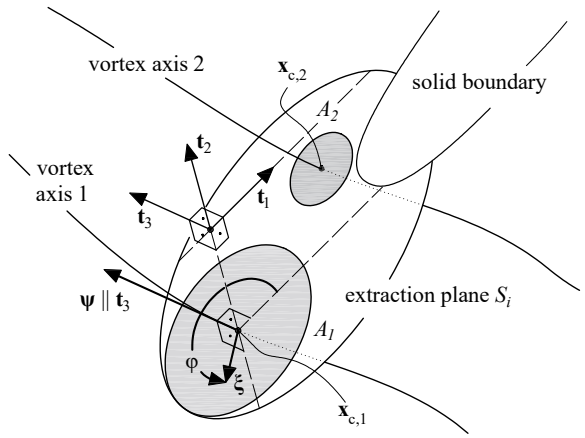

Figure 5: Local Cartesian coordinate system t_1, t_2 and t_3; local cylindrical coordinate system with the radial coordinate ξ, the azimuthal coordinate φ and the normal height coordinate ψ with $\boldsymbol{\psi} \parallel \mathbf{t}_3$.

As shown in Fig. 5, two local coordinate systems are used in the following:

(i) The local Cartesian coordinate system with the in-plane coordinates t_1 and t_2 and the coordinate t_3 pointing in the direction of the surface normal;

(ii) a local cylindrical coordinate system with the origin being the respective vortex center $\mathbf{x}_c$, the radial coordinate ξ, the azimuthal coordinate φ and the height coordinate ψ with $\boldsymbol{\psi} \parallel \mathbf{t}_3$.

In a first step, the centers $\mathbf{x}_{c,j}$ of the vortices crossing each extraction plane S_i have to be determined. The intuitive approach used here is based on the assumption that each vortex features a distinct pressure drop in its center. The developed algorithm checks three criteria in order to identify one or more vortex centers $\mathbf{x}_{c,j}$*:

(i) A local minimum of the pressure field is required at $\mathbf{x}_c = \mathbf{x}_c(t_{1,c}, t_{2,c}, 0)$:

$$c_p(\mathbf{x}_c) < c_p(\mathbf{x}), \tag{6}$$

for all $\mathbf{x}$ with $\|\mathbf{x} - \mathbf{x}_c\| \leq \delta_1$.

(ii) The pressure drop at $\mathbf{x}_c$ must exceed a certain threshold value $c_{p,\lim}$,

$$c_p(\mathbf{x}_c) < c_{p,\lim}, \tag{7}$$

(iii) and, in order to exclude boundary layer regions from the search, the distance δ to solid boundaries (wall distance) must exceed a certain threshold value δ_2:

$$\delta(\mathbf{x}_c) \geq \delta_2. \tag{8}$$

The threshold for the pressure drop $c_{p,\lim}$ as well as δ_1 and δ_2 constitute a set of parameters that has to be chosen with care in order to filter out unwanted results, i.e. local pressure minima that are obviously not associated to vortices.

Once one or more vortex centers are found for the extraction plane and along with it the pressure drop $c_{p,\min}$, the circulation Γ and radius of the viscous core r_a can be estimated from the flow field. The procedure described in the following is based on the Batchelor vortex model (or q-vortex), where the azimuthal velocity distribution is given by:

$$u_\varphi = \frac{\Gamma}{2\pi\xi}\left[1 - \exp\left(\frac{-\beta\xi^2}{r_a^2}\right)\right], \tag{9}$$

with the model constant $\beta = 1.256$ as well as the model parameters Γ and r_a (Devenport et al. 1996, e.g.).

For the estimate, geometrical and flow data is transformed to the cylindrical coordinate system previously mentioned. For each vortex j, a subset A_j is defined as illustrated in Fig. 5. The routine described in the following disregards all points that are not included in the subset.

In general, the velocity field in the vicinity of a vortex consists of the contribution due to the vortex itself and of the underlying "background" flow field that needs to be filtered out before the subsequent steps can be carried out. Since

*Since the procedure is the same for all vortices and extraction planes, the indices i and j are omitted unless they are necessary for better understanding.

the vortex is a very compact and discernible flow structure, it is justifiable to assume that the contribution of the background flow is more or less constant over A, which allows to identify the background velocity field as the averaged flow velocity in that region.

Extracting the azimuthal velocity for different angular positions at a given radial position and subsequent averaging leads to $\tilde{u}_\varphi = \tilde{u}_\varphi(\xi)$ and vanishing radial velocities $\tilde{u}_\xi$.

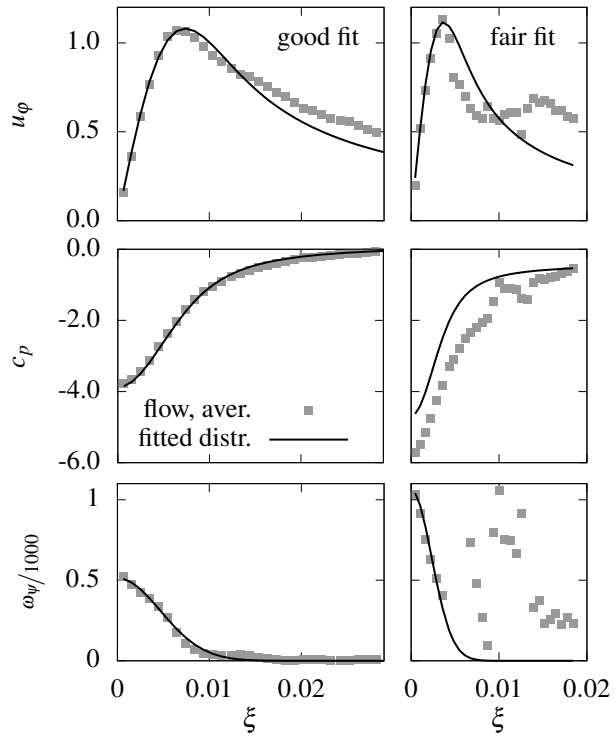

Figure 6: Evaluating circulation Γ and viscous core radius r_a by data fitting. Left-hand side: example for a good fit for a cross section of the trailing edge vortex; right-hand side: fair fit for a cross section of a leading edge vortex close to the blade surface.

In the second step, the circulation Γ and the viscous core radius r_a are found by data fitting. Here, Γ and r_a as parameters of the Batchelor vortex with $u_\varphi(\Gamma, r_a, \xi)$ are adjusted by applying a Gauss-Newton algorithm, so that:

$$\int \left[\tilde{u}_\varphi(\xi) - u_\varphi(\Gamma, r_a, \xi)\right] \mathrm{d}\xi \rightarrow \min. \tag{10}$$

The quality of the vortex flow approximation with the values for Γ and r_a determined in this way can be evaluated by reconstructing pressure and vorticity field.

By assuming $\partial/\partial\psi = 0$, $\partial/\partial\varphi = 0$, $u_\psi = 0$ and $u_\xi = 0$, it is possible to express the pressure field of the vortex by integrating the simplified momentum equation

$$\frac{\partial p}{\partial \xi} = \rho \frac{u_\varphi^2}{\xi}, \tag{11}$$

where u_φ is given by Eq. 9. With the same assumptions, one obtains the vorticity field of the vortex by taking the curl of the velocity:

$$\omega_\psi = \frac{1}{\xi} \frac{\partial(\xi u_\varphi)}{\partial \xi}. \tag{12}$$

Fig. 6 shows exemplary results of such an evaluation for two different extraction planes and vortex types. On the left-hand side of the diagram, results for a trailing edge vortex are shown. In this case, a good agreement between the actual flow field in terms of velocity, pressure and vorticity and the fitted flow field can be seen. Vortices close to the surface of the blade such as leading edge vortices cannot be captured with the same quality. Here, as shown on the right-hand side of the diagram, the agreement between actual and fitted flow field is not as accurate; however, it is still deemed acceptable. These examples stand for a general trend: the larger the distance between vortex and surface, the better the vortex can be represented by a fitted Batchelor vortex. For leading edge vortices and local tip vortices, the results are therefore afflicted with some uncertainties.

In some cases, it was necessary to determine circulation and viscous core radius manually. Evaluating Eq. 9 at $\xi = r_a$ and $\tilde{u}_{\varphi,\max} = \tilde{u}_\varphi(r_a)$ lead to:

$$\Gamma \approx 8.785 \tilde{u}_{\varphi,\max} r_a, \tag{13}$$

which allows to determine Γ and r_a based on the maximum of the azimuthal velocity.

Another important measure for studying the behaviour of leading edge and local tip vortices is the overall vorticity present in a given extraction plane S. In particular, it is interesting to analyse the integrated positive vorticity Ω^+ and the integrated vorticity of the opposite sign Ω^-:

$$\Omega^+ = \oiint_S \omega_3^+ \mathrm{d}S \tag{14}$$

and

$$\Omega^- = \oiint_S \omega_3^- \mathrm{d}S. \tag{15}$$

Within this work, Ω^+ is called the (positive) vorticity budget, whereas Ω^- is called the negative vorticity budget. Integration of the vorticity component ω_3 orthogonal to the respective extraction plane is carried out using the local Cartesian coordinate system t_1, t_2 and t_3. In order to only capture vorticity that is related to the formation of vortices, a threshold value ε is introduced. Further, regions within the boundary layer of the blade are excluded from the integration. With the parameter δ_2, which has already been used in the criterion posed by Eq. 8, one obtains

$$\omega_3^+ = \begin{cases} \omega_3 & \text{if } \omega_3 \geq \varepsilon \text{ and } \delta(\mathbf{x}) \geq \delta_2 \\ 0 & \text{else} \end{cases} \tag{16}$$

for the positive contribution, whereas for the negative contribution, it can be written analogously:

$$\omega_3^- = \begin{cases} \omega_3 & \text{if } \omega_3 \leq -\varepsilon \text{ and } \delta(\mathbf{x}) \geq \delta_2 \\ 0 & \text{else} \end{cases}. \tag{17}$$

Finally, the averaged level of vorticity $\overline{\omega}$ in the vortex core is introduced:

$$\overline{\omega} = \frac{\Gamma}{\pi r_a^2}. \tag{18}$$

Whereas Γ and $\Omega^{\pm}$ are measures for the strength of the vortex in terms of circulation and accumulated vorticity present within the vortex core and its surrounding, $\overline{\omega}$ can be used to characterise the distribution of vorticity.

2.5 Geometry Variation and Operation Conditions

To generate a variety of different flow configurations in the propeller tip region, six variants of a given, representative blade design were investigated at different advance ratios J. The main particulars of the baseline design A000 and the variants are listed in Tab. 1.

Table 1: Main dimensions of the baseline propeller A000 and variants.

Characteristics			**Value**
Propeller A000 (baseline)			
Type			CPP, twin screw
Propeller diameter	$D = 2R$	[m]	0.250
Number of blades	n_b	[-]	5
Hub ratio	d_h/D	[-]	0.287
Area ratio	$A_e/(\frac{\pi}{4}D^2)$	[-]	0.680
Pitch ratio	$P_{0.6}/D$	[-]	1.470
Pitch tip unloading		[%]	30.0
Skew angle		[deg]	35.0
Tip rake ratio	x_{tip}/D	[-]	0.0
Propeller A001 (variation of pitch: less tip unloading)			
Pitch ratio	$P_{0.6}/D$	[-]	1.405
Pitch tip unloading		[%]	10.0
Propeller A002 (variation of pitch: higher tip unloading)			
Pitch ratio	$P_{0.6}/D$	[-]	1.525
Pitch tip unloading		[%]	50.0
Propeller A003 (variation of rake: tip towards SS)			
Tip rake ratio	x_{tip}/R	[-]	−0.110
Propeller A004 (variation of rake: tip towards SS)			
Tip rake ratio	x_{tip}/R	[-]	−0.055
Propeller A005 (variation of rake: tip towards PS)			
Tip rake ratio	x_{tip}/R	[-]	0.055
Propeller A006 (variation of rake: tip towards PS)			
Tip rake ratio	x_{tip}/R	[-]	0.110

Even though the structures of the leading edge vortex and the local tip vortex depend on geometrical details such as leading edge radius, the shape of the propeller tip edges, as well as on thickness and camber in the tip region, we focused in the present study on two main parameters – tip unloading and tip rake. Other design parameters were left to future research, as the present study would otherwise have become too extensive.

The baseline design A000 was investigated at five different operation conditions (see Tab. 2) ranging from the design point at $J = 1.08$ down to $J = 0.85$. For the variants A001 to A006, only two operation conditions were applied. All variants were designed to deliver the same thrust for $J = 0.85$.

The simulations were carried out in model scale, leading to a Reynolds number of $\text{Re}_{0.9} = 0.9\pi nDc_{0.9}\nu^{-1} = 9.0 \cdot 10^5$ with $c_{0.9}$ being the chord length at $r/R = 0.9$ and ν the kinematic viscosity of water.

Table 2: Operation conditions for propeller A000 and variants. Homogeneous inflow, variation of advance velocity.

Characteristics			**Value**
Propeller A000 (baseline)			
Advance coeff.	J	[-]	0.85, 0.9075, 0.965, 1.0225, 1.08
Number of rev.	n	[s^{-1}]	15.0
Reynolds number	$\text{Re}_{0.9}$	[-]	$9.0 \cdot 10^5$
Propeller A001 – A006 (variants)			
Advance coeff.	J	[-]	0.85, 1.08

3 FLOW FEATURES

For a better understanding of the results presented in Section 4, some typical flow features encountered during the study are discussed below using the baseline propeller A000 at $J = 0.85$ as example.

Results in terms of vorticity ω_3 and pressure c_p are depicted in Figs. 7 and 8, following the direction of the spanwise flow for selected stations along the leading edge (planes 16 and 14), the propeller tip (planes 10, 9, 7 and 6) as well as downstream the trailing edge (planes 4 and 2). It is recommended to view the figures using a monitor and not in printed form, as the color scale is usually better reproduced here.

For each cross section shown in the figures, the locations of pressure minima are denoted by a red star $\star$ labelled with a number indicating the strength of the pressure minimum. Here, the index 0 stands for the dominant pressure minimum and the index 1 for the second minimum. In some cases, there are more than two prominent minima; however, these cases are not discussed.

At this point, if two or more vortices cross an extraction plane, the vortex with the strongest pressure drop in its center is declared as *dominant*. This is mostly (but not necessarily) the vortex with the highest circulation. Hence, the dominant vortex will be labelled with the index 0 for a given cross section. However, depending on its development and the development of the co-existing partners, the index might be different for another cross section.

Reverting to the example and Fig. 7, it can be seen that, for the cross section in plane 16 (at about $r/R = 0.9$), leading edge separation occurs. In particular, a shear layer is visible, winding up into a leading edge vortex with a local pressure minimum in its core.

A common feature that can be observed, is the generation of a region of negative vorticity (i.e. of opposite sign) between the feeding shear layer and the leading edge vortex. The occurrence of this secondary flow pattern is very typical for leading edge vortices and has also been described by other authors (Eldredge and Jones 2019, e.g.). In particular, entrainment of negative vorticity is believed to be

a mechanism that, apart from spanwise convection of vorticity along the leading edge, balances the vorticity originating from the feeding shear layer and thus regulates the growth of the leading edge vortex (Wojcik and Buchholz 2014).

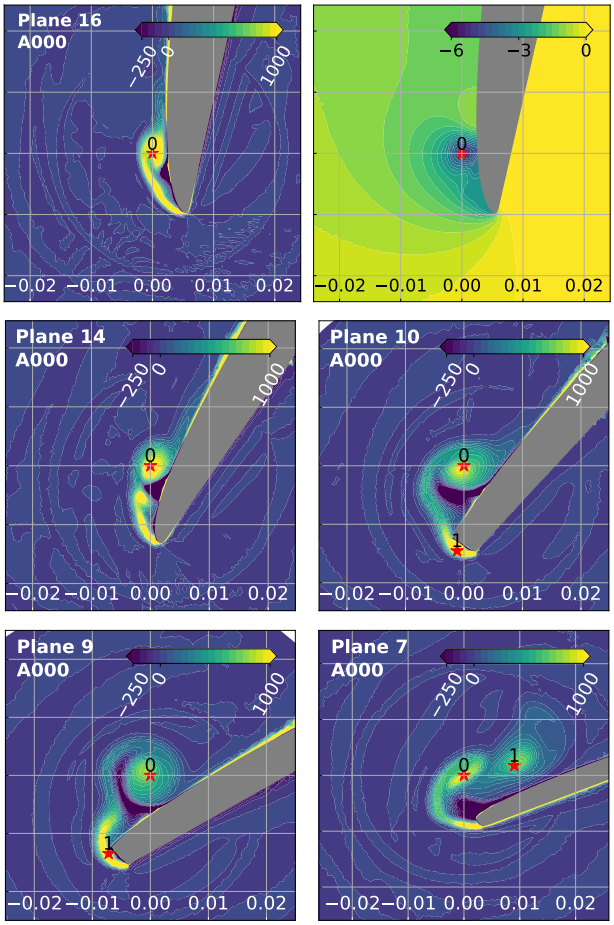

Figure 7: Distribution of vorticity ω_3 in the range from -250.0 to 1000.0 for different cross sections along leading edge and propeller tip. Pressure coefficient c_p in the range from -6.0 to 0.0 for plane 16 only. Baseline propeller A000 at $J = 0.85$. Red stars $\star$ mark locations of local pressure minima. See text for further explanation.

Following the spanwise flow along the leading edge (planes 14 and 10), the leading edge vortex gains strength by accumulating more vorticity while the distance to the blade surface increases and the cross section becomes more circular. Eventually, as it can be observed in plane 9, the region of negative vorticity is stretched and deformed to a layer, weakening the link between feeding shear layer and leading edge vortex. At the same point, the local tip vortex starts to develop (index 1 in plane 10 and plane 9). Further downstream (plane 7), the local tip vortex has gained enough strength to coexist with leading edge vortex. In this particular case, the pressure drop in the core of the local tip vortex (now index 0 instead of 1) is higher than for the leading edge vortex (now index 1).

Leaving the trailing edge (planes 6, 4 and 2 in Fig. 8), both vortices merge into the trailing vortex. The region of negative vorticity mentioned before as well as the vorticity shed from the trailing edge take part in the process. Plane 2 (bottom row of the figure) is located approximately one chord length downstream of the propeller tip. As the concentric isolines of the pressure field indicate, the merging process appears to be completed quite close to the propeller tip.

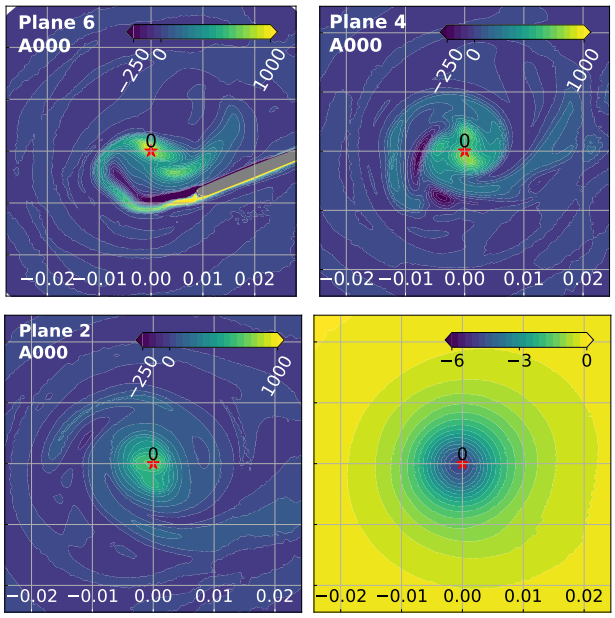

Figure 8: See Fig. 7. Cross sections at the propeller tip and further downstream. Pressure coefficient c_p for plane 2 only. Plane 2 is located approximately one chord length ($c_{0.9}$ at $r/R = 0.9$) downstream of the propeller tip.

4 RESULTS

4.1 Grid Study

The basic setup for the viscous simulations using *Star-CCM+* and the pursued meshing strategy have been described in Sections 2.1 and 2.2. In order to investigate the influence of discretisation, a grid study was carried out. Five different meshes with varying number of cells ranging from 4.0 M (mesh M4cc) to 76.0 M cells per blade (mesh M0cc) were tested. For the grid study, the case of the baseline propeller A000 operated at $J = 0.85$ was used.

The grid convergence behaviour is evaluated both by integral forces and by vortex flow characteristics at the blade tip. Whereas integral forces such as thrust and torque differ not more than 1.5 % when comparing the results originating from the finest mesh to the ones obtained by the coarser meshes, it is much more difficult to achieve convergence when it comes to flow details of the vortex flow in the blade tip region. The same observation was made by Peric (2022).

Results for an extraction plane downstream of the blade tip capturing the developing trailing vortex (TRV) are depicted on the right hand side of Fig. 9. Here, it can be stated that increasing the resolution from 26.1 M cells (M1cc) to 76.0 M cells (M0cc) does not lead to significant changes.

Table 3: Different mesh refinement levels used in the grid study.

Characteristics		Value
Mesh M0cc (finest)		
Number of cells per blade	N_{cell}	76.0 M
	$\log(N_{\text{cell}})$	7.88
Cells within vortex core rad.	$N_{\text{cell,vortex}}$	17 … 21
Mesh M1cc (fine)		
Number of cells per blade	N_{cell}	26.1 M
	$\log(N_{\text{cell}})$	7.41
Cells within vortex core rad.	$N_{\text{cell,vortex}}$	13 … 15
Mesh M2cc (medium)		
Number of cells per blade	N_{cell}	11.4 M
	$\log(N_{\text{cell}})$	7.05
Cells within vortex core rad.	$N_{\text{cell,vortex}}$	10 … 12
Mesh M3cc (coarse)		
Number of cells per blade	N_{cell}	6.2 M
	$\log(N_{\text{cell}})$	6.79
Cells within vortex core rad.	$N_{\text{cell,vortex}}$	9 … 10
Mesh M4cc (coarsest)		
Number of cells per blade	N_{cell}	4.0 M
	$\log(N_{\text{cell}})$	6.60
Cells within vortex core rad.	$N_{\text{cell,vortex}}$	8 … 9

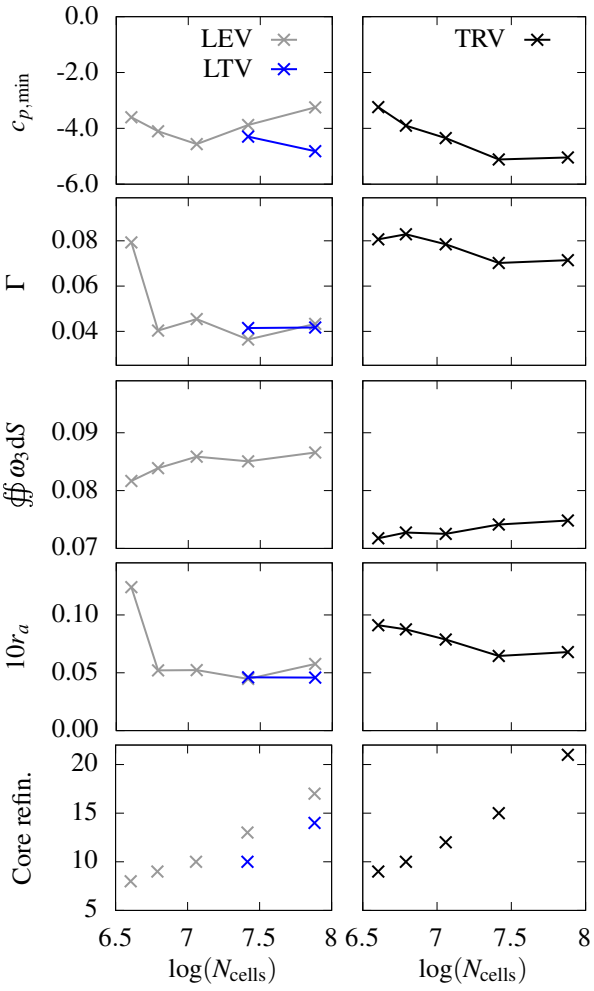

Figure 9: Grid convergence behaviour with respect to different vortex quantities and core refinement (lowest diagram).

On the left-hand side of the figure, the convergence behaviour for vortex quantities determined for an extraction plane located in the blade tip region with prevailing leading edge vortex and local tip vortex is shown. In this case, the situation is different. Even though, the overall amount of vorticity $\oiint \omega_3 \mathrm{d}S$ does not change significantly when comparing the results for meshes M2cc, M1cc and M0cc, the *distribution* of vorticity is significantly affected by the mesh resolution. Whereas simulation results obtained with mesh M4cc, M3cc and M2cc show only one vortex (local tip vortex and leading edge vortex smeared into one single vortex), it requires a much finer mesh resolution to obtain two distinct vortices. For further illustration, the distribution of vorticity ω_3 and pressure c_p is depicted in Fig. 10 for M3cc, M1cc and M0cc.

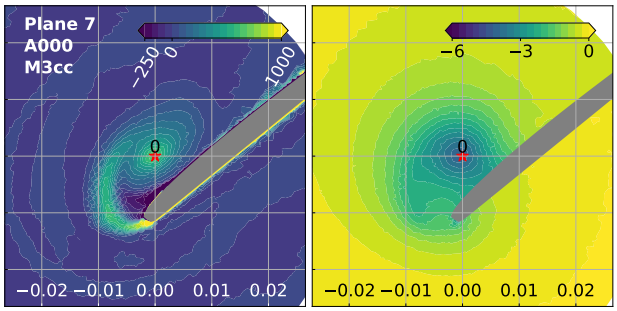

(a) Coarse mesh M3cc.

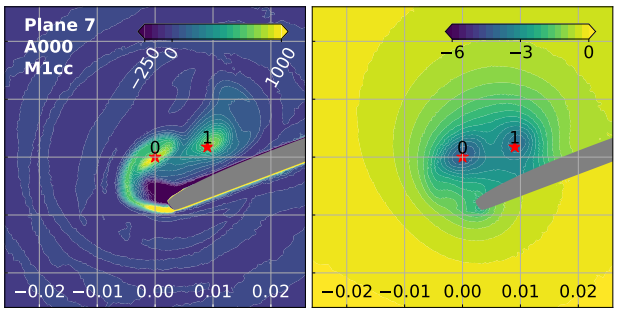

(b) Fine mesh M1cc.

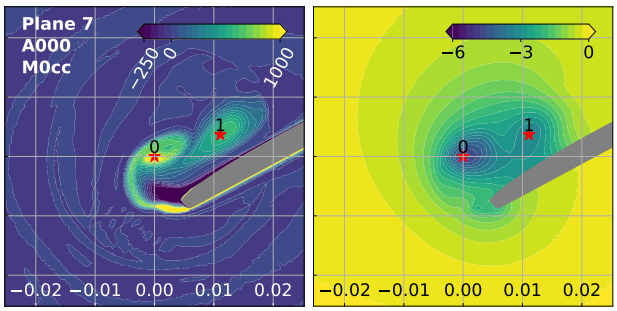

(c) Finest mesh M0cc.

Figure 10: Distribution of vorticity ω_3 (left-hand side of the subfigures) and pressure coefficient c_p (right-hand side) for different mesh refinement levels. Baseline propeller A000 at $J = 0.85$; plane 7 located at the blade tip. Red stars $\star$ mark locations of local pressure minima. See Section 3 for explanation.

In particular, reaching convergence with respect to the pressure drop $c_{p,\min}$ in the center of leading edge vortex and local tip vortex is challenging for the given case. Nevertheless, for the rest of the study, mesh M1cc was applied since it resolves relevant flow patterns to a satisfactory level while still allowing for investigating a considerable amount of different propeller variants and operation conditions.

4.2 Influence of Blade Load

In order to approximate the influence of the fluctuating blade load in the ship's wake field on the vortex structures at the blade tip, the baseline propeller A000 is investigated at five different advance ratios (see Tab. 2).

The diagrams shown in Fig. 11 depict selected vortex parameters such as pressure drop in the vortex core $c_{p,\min}$, circulation Γ, viscous core radius r_a, distance of the vortex core to the blade surface δ, the averaged level of vorticity in the vortex core $\overline{\omega}$, the ratio between positive and negative vorticity budget Ω^-/Ω^+ as well as k_T and η. Vortex parameters are analysed in the propeller tip region (plane 7) with prevailing local tip vortex (LTV) and leading edge vortex (LEV) as well as downstream of the propeller tip (plane 4), after merging into the trailing vortex (TRV). Corresponding flow patterns are shown in Figs. 12 and 13.

Obviously, when decreasing the advance ratio, the blade load in terms of k_T increases, and, while moving away from the design point, the efficiency η falls. With increasing blade load, the pressure drop $c_{p,\min}$ in the core of the trailing vortex (TRV) gets more extreme. It changes more or less linearly with increasing blade load for a wide range of operation conditions. Interestingly, when approaching $J = 0.9075$, the curve becomes noticeable flatter, even though, the circulation of the trailing vortex increases beyond proportion to more than 60 % of the blade circulation Γ_b.

How can this be explained? To answer this question, it is necessary to have a look at the vortex structures at the blade tip. For all advance ratios considered here, a discernible local tip vortex (LTV) reaching up to one third of the blade circulation is present. Somewhere between $J = 0.965$ and $J = 0.9075$, a leading edge vortex (LEV) rises, co-existing with the local tip vortex.

For operation conditions with only the local tip vortex being present, the local tip vortex transitions into the trailing vortex. Once the leading edge vortex occurs, it has a great impact on the flow at the blade tip and the structure of the trailing vortex. Instead of the local tip vortex transitioning into the trailing vortex, now, leading edge vortex and local tip vortex merge into the trailing vortex. This process takes place in the blade tip region (see Fig. 12).

Meunier et al. (2005) explain and discuss in detail the merging process of two co-rotating vortices with equal strength. They show that, depending on vortex configuration and Reynolds number, the square of the viscous core radius r_a^2 of the vortices before and after merging can differ by a factor of up to 3.5. Indeed, their work is based on idealised vortices that deviate in many details from the present flow configuration; however, the increase of viscous core radius r_a can be observed in the present case as well.

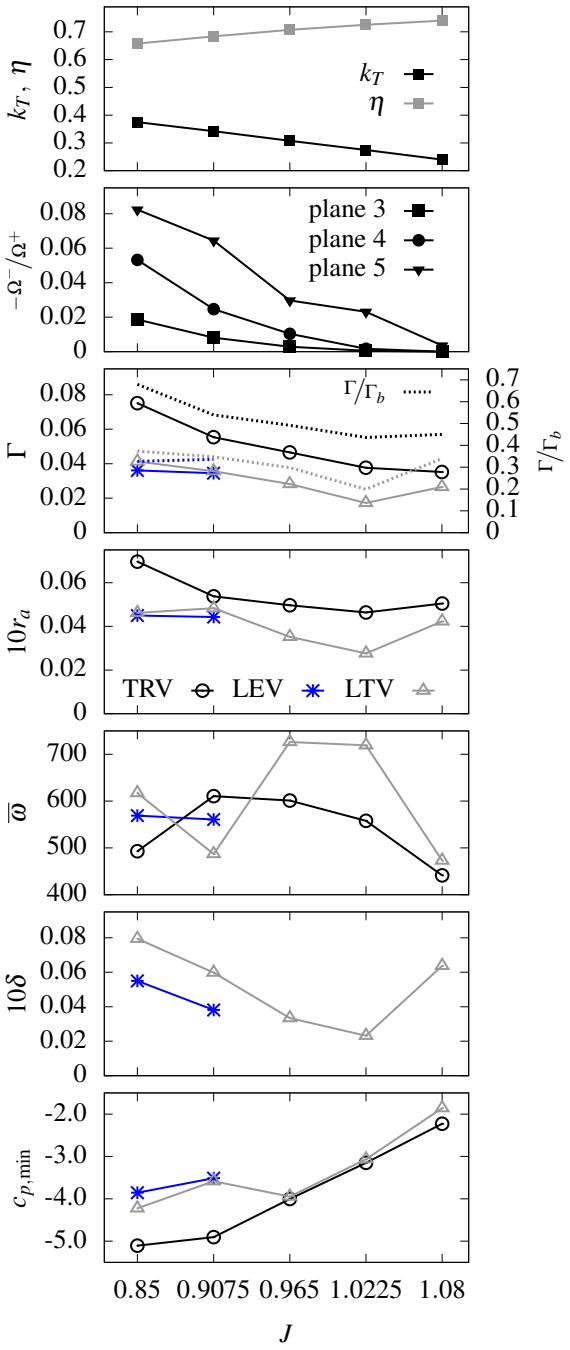

Figure 11: Influence of advance coefficient J on vortex quantities for local tip vortex (LTV) and leading edge vortex (LEV) evaluated in plane 7 as well as for the trailing vortex (TRV) evaluated in plane 4. Propeller A000.

Whereas the viscous core radius of the trailing vortex is at around 0.005 for advance coefficients down to $J = 0.965$, it becomes nearly 0.007 for $J = 0.85$, where leading edge vortex and local tip vortex with a viscous core radius of approx. 0.0045 merge into the trailing vortex. A consequence is that the level of vorticity $\overline{\omega}$ in the trailing edge vortex noticeably falls from around 600.0 to 440.0 at $J = 0.85$.

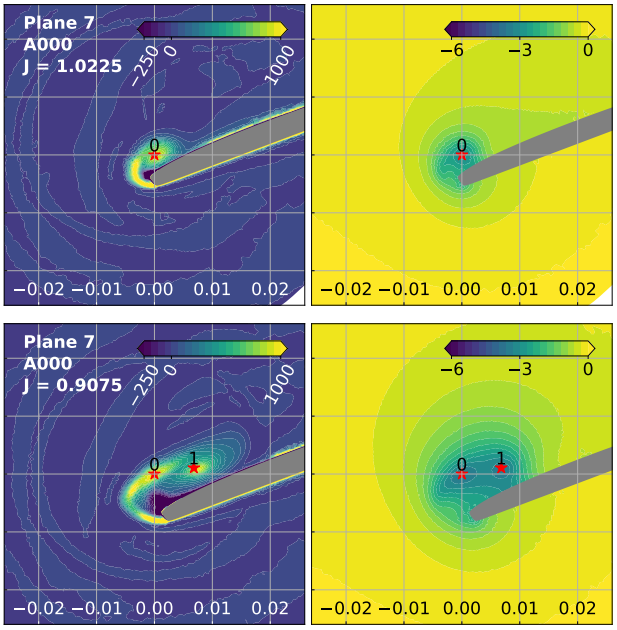

Figure 12: Distribution of vorticity ω_3 and pressure coefficient c_p for a cross section in the tip region (plane 7) for different advance ratios J. Baseline propeller A000. Red stars ⋆ mark locations of local pressure minima. See Section 3 for explanation.

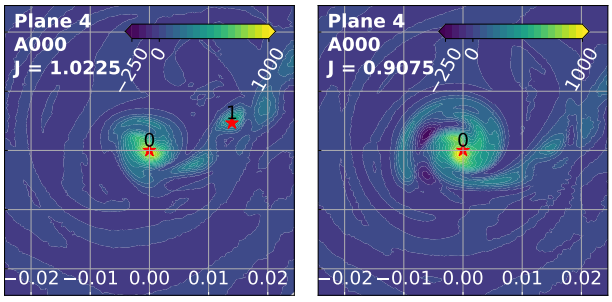

Figure 13: See Fig. 12. Distribution of vorticity ω_3 for a cross section downstream of the propeller tip (plane 4) for different advance ratios J.

Apart from merging, there is another effect. As discussed in Section 3, together with the leading edge vortex, a considerable amount of negative vorticity is produced forming a coherent region between feeding shear layer and leading edge vortex. Further downstream, this region becomes stretched and takes part in the merging process. When looking at Fig. 13 for the case of $J = 0.9075$, remnants of this secondary flow structure are still discernible.

In Fig. 11, the ratio between negative and positive vorticity budget Ω^+/Ω^- for planes 5, 4 and 3 downstream of the propeller tip is plotted over the advance ratio. Not surprising, the ratio decays from plane 5 to plane 3 as the merging progresses. The ratio increases notably in all three cross sections with the leading edge vortex being present at lower advance ratios. It can therefore be assumed that the entrainment of negative vorticity has a further dampening effect on the levels of vorticity reached in the trailing vortex.

4.3 Influence of Blade Geometry

In the present section, it is investigated how applying geometrical changes to the baseline propeller affects the vortex structures at the propeller tip. The applied changes comprise a variation of tip rake as well as tip unloading (see Tab. 1). All variants were considered at design condition $J = 1.08$ and at $J = 0.85$. In most cases, the higher blade load at $J = 0.85$ gives rise to a leading edge vortex and a pronounced local tip vortex.

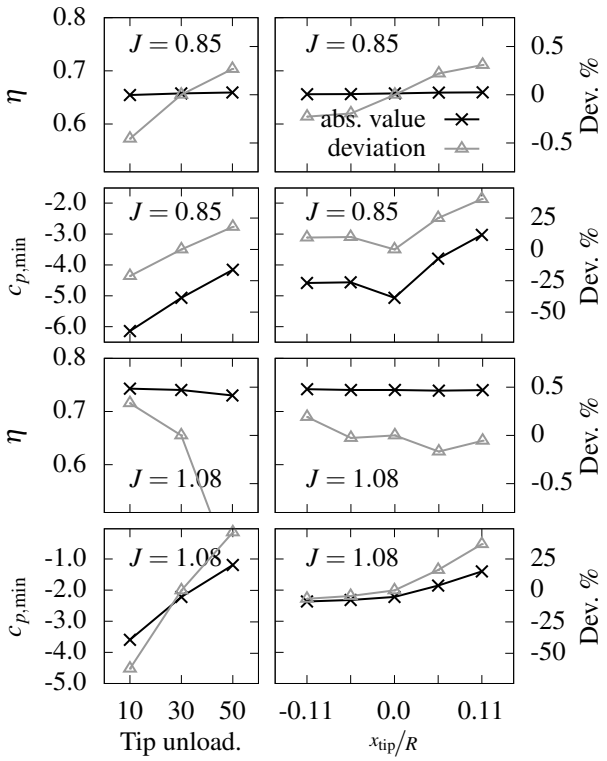

Figure 14: Influence of tip unloading and tip rake on efficiency η and pressure drop in the core of the trailing vortex $c_{p,\min}$ evaluated in Plane 4 for $J = 0.85$ (upper half of the figure) and $J = 1.08$ (lower half).

Global performance parameters such as load distribution $k_{T,r}$, efficiency η and pressure drop in the core of the trailing vortex $c_{p,\min}$ are presented in Figs. 14 and 15.

As a general tendency, it can be observed that changing tip rake has only a minor effect on the load distribution as well on the efficiency, both for $J = 1.08$ and for $J = 0.85$. Changes in efficiency are below 0.4 % compared to the baseline design. On the other hand, the effect on the pressure drop in the vortex core is considerable.

In order to obtain a similar reduction of the pressure drop by applying tip unloading, one has to accept much higher changes of the load distribution and losses in efficiency at the design operation condition. Therefore, applying tip rake is a very interesting alternative to tip unloading when it comes to designing efficient and propellers with high cavitation inception speed.

To explore this further, it is necessary to have a closer look at the tip flow and the behaviour of the vortex structures.

The diagrams in Figs. 17 and 18 depict relevant vortex quantities analysed for different extractions planes in the leading edge region (planes 14 to 12), the tip region (planes 11 to 6) and downstream of the leading edge (planes 5 to 3). Here, results for $J = 0.85$ are shown. In all cases, plane 3 is located not more than one chord length ($c_{0.9}$ at $r/R = 0.9$) downstream of the propeller tip. Flow details in terms of vorticity ω_3 and pressure c_p are depicted for selected extractions planes in Figs. 16 and 19. Fig. 25 at the end of the paper shows flow details for all propeller variants for a wider selection of planes making it possible to compare flow features and to follow the evolution of vortex structures for different variants.

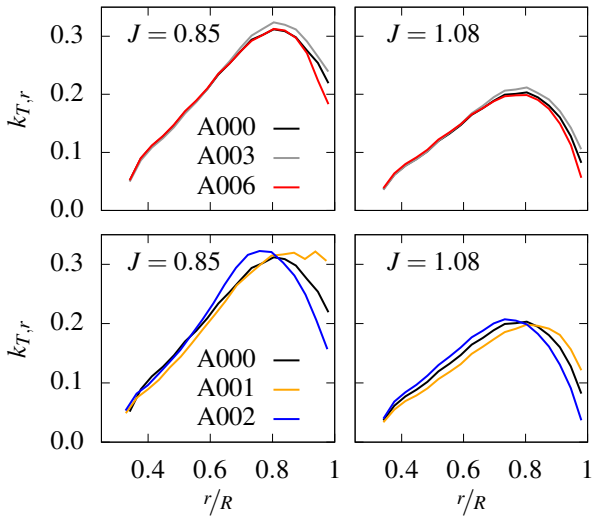

Figure 15: Radial distribution of thrust $k_{T,r}$ for baseline propeller A000 and variants A001, A002, A003 as well as A006 for $J = 0.85$ and $J = 1.08$.

First, the influence of unloading the blade tip is investigated and commented on. Tip unloading is a classical and well-understood concept to control the strength of the trailing vortex and to increase cavitation inception speed. Reducing the pitch leads to less blade load and less circulation bound to the blade and consequently to less vorticity that can feed vortices at the propeller tip. This is exactly what can be seen in Fig. 17. For A002, the propeller variant with a high tip unloading of 50 %, only a small vorticity budget Ω^+ is provided at the propeller tip, and a small compact local tip vortex is generated. Leading edge separation does not occur and therefore no leading edge vortex emerges. With decreased tip unloading (30 % for the baseline propeller A000 and 10 % for variant A001), leading edge separation sets in, the vorticity budget Ω^+ becomes larger and the strength Γ of the vortex structures increases. A leading edge vortex is formed for A000, however, at the tip, the local tip vortex is still dominating (see Fig. 16b). For variant A001, the leading edge vortex is prevailing for all locations along the propeller tip, whereas the local tip vortex appears to be absorbed by the shear layer feeding the leading edge vortex (see Fig. 16c).

In this case, as the pressure drop $c_{p,\min}$ in the core of the leading edge vortex is clearly more extreme than it is the case for the trailing vortex (see Fig. 17), the onset of vortex cavitation will occur in the leading edge region and not in the trailing vortex.

Even though the levels of vorticity $\overline{\omega}$ fall when decreasing the tip unloading, the overall amount of vorticity grows to such an extend that the pressure drop $c_{p,\min}$ in the vortex cores is much more pronounced for variant A001 than for the baseline propeller A000 and variant A002.

In other words, for the given example of tip unloading, the dominating effect regulating the pressure drop in the vortex core is the overall amount of vorticity (the vorticity budget) and the circulation – and not the distribution of vorticity.

When it comes to the influence of rake, the situation is different. As shown in Figs. 14 and in Fig. 18, for positive rake (variant A006, rake towards the pressure side) the effect on the pressure drop $c_{p,\min}$ is remarkable.

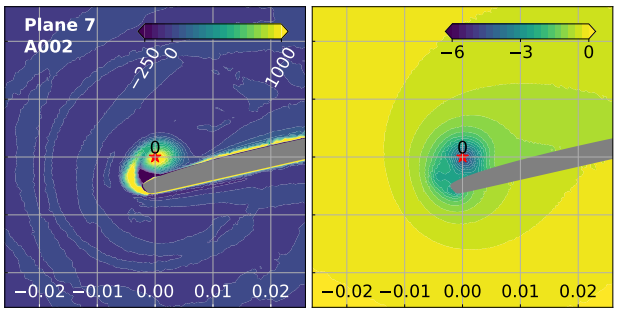

(a) Variant A002 (tip unloading 50.0 %).

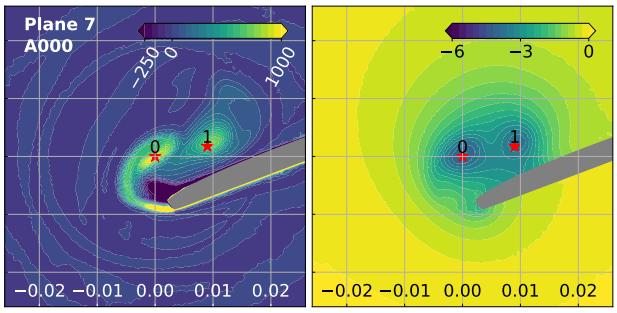

(b) Baseline propeller A000 (tip unloading 30.0 %).

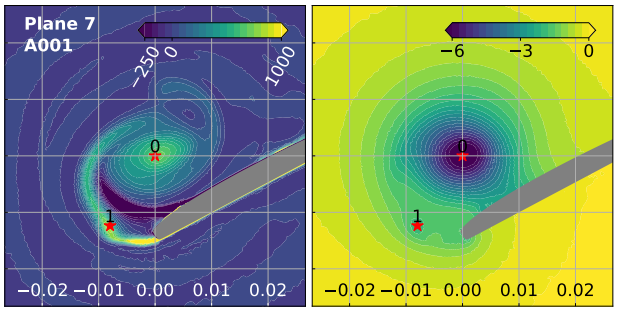

(c) Variant A001 (tip unloading 10.0 %).

Figure 16: Distribution of vorticity ω_3 (left-hand side of the subfigures) and pressure coefficient c_p (right-hand side) baseline propeller A000, variant A001 and variant A002 at $J = 0.85$; plane 7 located at the blade tip. Red stars $\star$ mark locations of local pressure minima. See Section 3 for explanation.

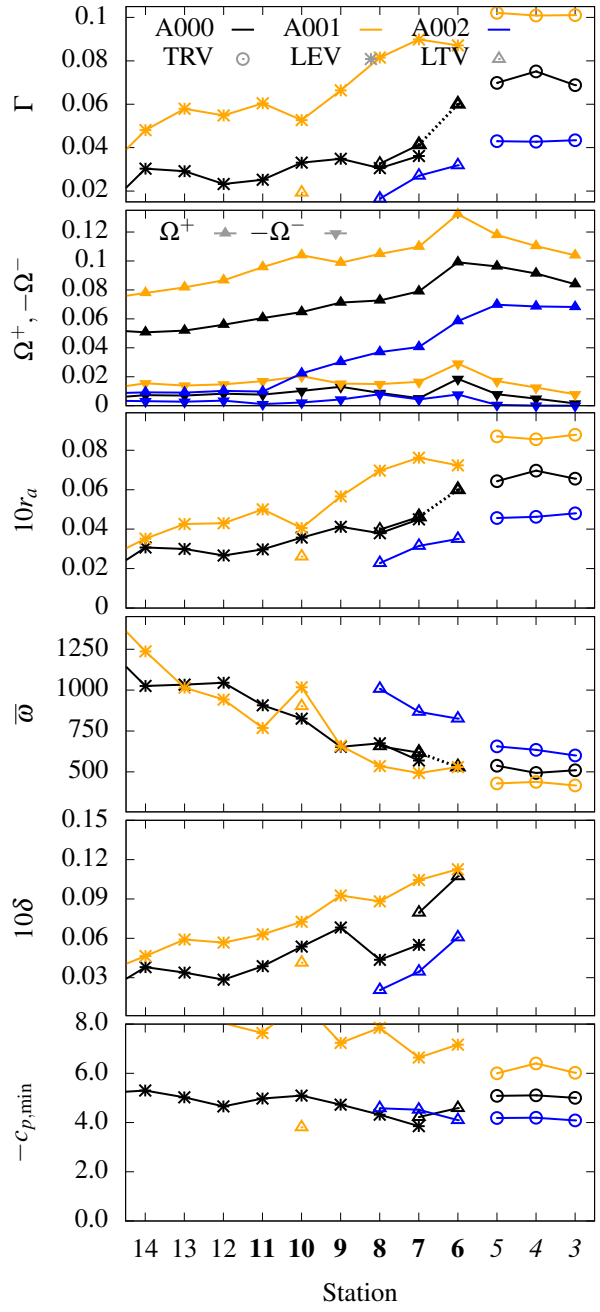

Figure 17: Influence of tip unloading on vortex quantities for local tip vortex (LTV), leading edge vortex (LEV) as well as for the trailing vortex (TRV) evaluated at different extraction planes along the leading edge (planes 14 to 12), propeller tip (planes **11** to **6**) and downstream of the propeller tip (planes *5* to *3*). Baseline propeller A000 (tip unloading 30.0%), variant A001 (tip unloading 10.0% and variant A002 (tip unloading 50.0%) at $J = 0.85$. Dotted lines indicate that vortex quantities were evaluated manually.

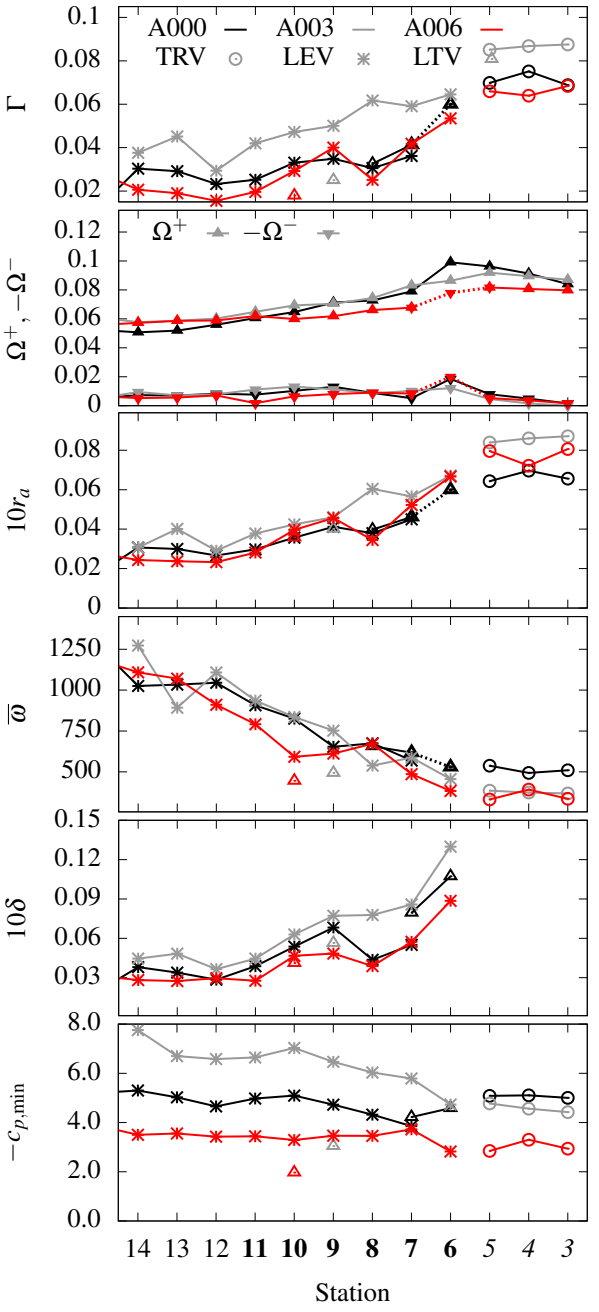

Figure 18: See Fig. 17. Influence of tip rake x_{tip}/R on vortex quantities. Baseline propeller A000 ($x_{tip}/R = 0.0$), variant A003 ($x_{tip}/R = -0.11$, tip towards suction side) and variant A006 ($x_{tip}/R = 0.11$, tip towards pressure side).

On the other hand, the blade load distribution and the vorticity budget Ω^+ remain more or less unaffected compared to the scenario with varying tip unloading (see also Amini et al. 2019). The underlying cause must therefore be sought in the flow details at the blade tip and the *distribution* of vorticity.

When examining Figs. 19a and 19c, it is striking that only a leading edge vortex is present. By applying tip rake, the flow from pressure side to suction side around the propeller tip can be steered in such way that the local tip vortex is suppressed or at least not discernible from the feeding shear layer.

Depending on the direction of rake, the characteristics of the leading edge vortex differ for the given examples. For variant A003 (rake towards suction side), the vortex center is clearly located further away from the blade surface than it is the case for the other configurations.

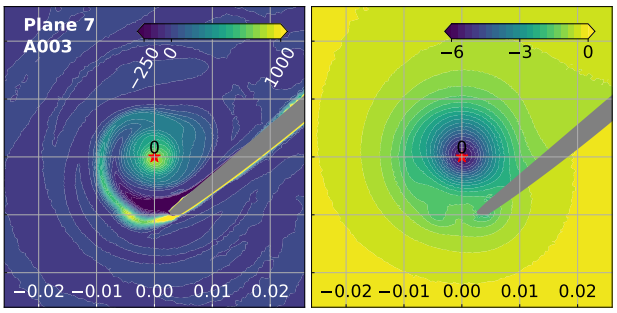

(a) Variant A003 (tip rake $x_{tip}/R = -0.11$).

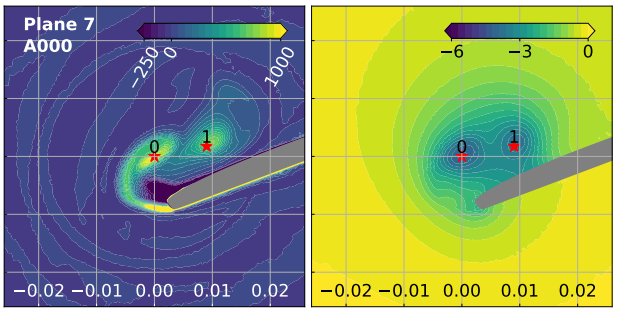

(b) Baseline propeller A000 (tip rake $x_{tip}/R = 0.0$).

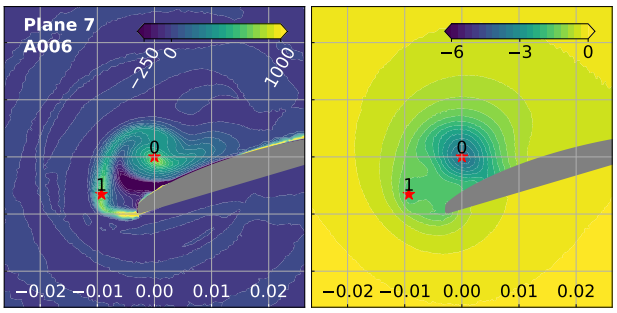

(c) Variant A006 (tip rake $x_{tip}/R = 0.11$).

Figure 19: See Fig. 16. Baseline propeller A000, variant A003 and variant A006 at $J = 0.85$.

Compared to variant A006 (rake towards pressure side), the cross section of the leading edge vortex is quite circular, which might be explained by the greater distance to the wall. Apparently, the "undisturbed" vortex accumulates vorticity more effectively which leads to a higher circulation Γ and a higher levels of vorticity compared to the leading edge vortex of variant A006. For the latter, both the circulation and the levels of vorticity are significantly lower.

For the vorticity level $\overline{\omega}$ and the pressure drop $c_{p,\min}$ in the trailing vortex downstream of the propeller tip, the absence of a compact and "sharp" local tip vortex clearly has a dampening effect mitigating cavitation inception. This analysis is continued in a more systematic manner in the next section.

4.4 Vortex Characteristics

So far, it has been shown that the pressure drop in the core of the trailing vortex is affected by both the overall amount of vorticity being present (the vorticity budget) and the level of vorticity in the vortex core, i.e. the distribution of vorticity. In Sections 3 and 4, three effects reducing the level of vorticity have been encountered: (i) merging of local tip vortex and leading edge vortex, (ii) entrainment of an increased amount of negative vorticity and (iii) suppression of the local tip vortex, i.e., the leading edge vortex transitions into the trailing vortex. While only selected results were discussed in the previous sections, in the following the entirety of the simulation results are used to systematically identify mechanisms that reduce the vorticity levels. In the scatter plot in Fig. 20, each point represents data retrieved for a particular vortex cross section for a given variant and a given operation condition.

For the analysis, depending on the details of the tip flow, trailing edge vortices observed during this study can be divided into four categories:

(I) No leading edge vortex, only a local tip vortex is present.

(II) Only a strong leading edge vortex is present, the local tip vortex is suppressed or disappears in the feeding shear layer.

(III) Leading edge vortex and local tip vortex are coexisting, local tip vortex dominates.

(IV) Leading edge vortex and local tip vortex are coexisting, leading edge vortex dominates.

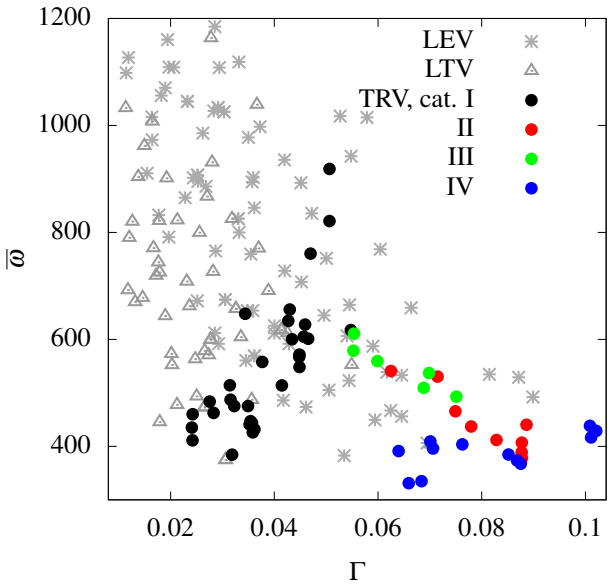

Figure 20: Correlation between Γ and $\overline{\omega}$ for leading edge vortices (LEV), local tip vortices (LTV) and trailing vortices (TRV). Vertical axis limited to 1200.0; values larger than 2000.0 were observed for LEV and LTV.

Fig. 20 shows the vorticity level $\overline{\omega}$ plotted over the vortex circulation Γ for leading edge vortices (LEV), local tip vortices (TRV) and the four categories of trailing vortices (TRV). Whereas the levels of vorticity can become relatively high for leading edge vortices and local tip vortices,

especially for small values of Γ, for trailing vortices, the vorticity levels clearly depend on the respective formation process.

Trailing vortices that originate from a local tip vortex (category I) can reach high levels of vorticity as well. This is no surprise, since none of the three mitigating effects mentioned before applies.

As soon as a leading edge vortex takes part in the formation process, vorticity levels become smaller. Category-III trailing vortices (a dominant local tip vortex merged with a co-existing leading edge vortex) exhibit lower levels of vorticity compared to category-I trailing vortices. Here, as discussed in detail in Section 3, the effect of merging and the entrainment of negative vorticity lead to reduced levels of vorticity in the core of the trailing vortex.

Further reduction of the vorticity level is observed for cases where only a leading edge vortex is present while the local tip vortex is suppressed (category II). This configuration could be observed for propeller variants A003 and A006 discussed in Section 4. Apart from entrainment of an increased amount of negative vorticity that comes with the leading edge vortex, another effect plays a role: the viscous core radius of the leading edge vortex transitioning into the trailing vortex can become relatively large as it grows along the leading edge. In contrast to that, local tip vortices – as the name indicates – are formed locally at the tip and are usually very compact.

Consequently, the lowest levels of vorticity are observed for a dominant leading edge vortex merging with a coexisting local tip vortex as it is the case for category-IV trailing vortices.

5 COMPARISON WITH EXPERIMENTAL DATA

Finally, the findings of the previous sections are underpinned by experimental data obtained during a cavitation inception test conducted in the depressurised towing tank of the Maritime Research Institute Netherlands (MARIN). Being part of an actual executed project, no specific details can be given regarding the operating point and geometry of the propeller.

Originally, the propeller was tested for design conditions as given for setting B001 in Tab. 4. Here, inception of vortex cavitation in the blade tip region was observed at $V_{\text{inc},1}$. With the intention to increase the cavitation inception speed, it was decided to repeat the test with a reduced pitch setting and increased number of revolutions (setting B002). Since $\Gamma_b \propto Tn^{-1}D^{-2}$ (Isay 1991), it was assumed that along with the blade circulation Γ_b, the circulation of the vortices in the blade tip region will decrease as well leading to a higher inception speed.

Surprisingly, exactly the opposite happened. Instead of increasing, the inception speed went from $V_{\text{inc},1}$ down to $V_{\text{inc},2} = 0.885\,V_{\text{inc},1}$.

In order to shed light on the reason for this unexpected result, the analysis techniques used in the previous sections are now applied to the flow details at the blade tip of propeller B000 when operating in setting B001 and B002.

Table 4: Main dimensions of Propeller B000. Pitch setting and operation conditions for setting B001 and B002 at inception speed for local tip vortex and trailing vortex cavitation.

Characteristics			**Value**
Propeller B000			
Type			CPP, twin screw
Propeller diameter	$D = 2R$	[m]	0.250
Number of blades	n_b	[-]	5
Hub ratio	d_h/D	[-]	0.287
Area ratio	$A_e/(\frac{\pi}{4}D^2)$	[-]	0.680
Pitch ratio	$P_{0.6}/D$	[-]	1.499
Pitch tip unloading		[%]	30.0
Skew angle		[deg]	45.0
Tip rake ratio	x_{tip}/D	[-]	0.0
Setting B001 (design pitch) at LTV/TRV cavitation inception speed			
Blade rotation angle		[deg]	0.0
Advance coeff.	J	[-]	1.139
Wake peak adv. coeff.	J_{peak}	[-]	0.870
Thrust coeff.	k_T	[-]	0.201
Cavitation inc. speed	V_{inc}		$V_{\text{inc},1}$
Setting B002 (reduced pitch) at LTV/TRV cavitation inception speed			
Blade rotation angle		[deg]	-4.75
Advance coeff.	J	[-]	0.987
Wake peak adv. coeff.	J_{peak}	[-]	0.756
Thrust coeff.	k_T	[-]	0.145
Cavitation inc. speed	V_{inc}		$0.885\,V_{\text{inc},1}$

Simulations where carried out at the respective inception speeds $V_{\text{inc},1}$ and $V_{\text{inc},2}$. For simplicity, the simulations were again performed in homogeneous inflow. In both cases, B001 and B002, an equivalent advance ratio J_{peak} was determined, taking into account the local axial and tangential inflow velocity components of the wake field in the tip region of the propeller and for the blade position with the highest blade load. The obtained values are listed in Tab. 4.

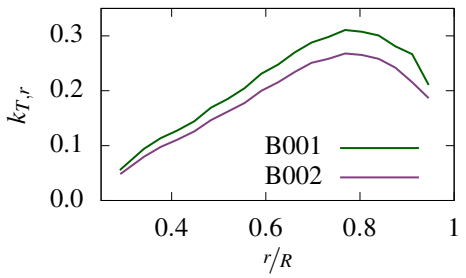

Figure 21: Radial distribution of thrust $k_{T,r}$ for propeller B000 in setting B001 and setting B002 as in Tab. 4.

Indeed, when comparing setting B001 and B002, one notices that the blade load is substantially lower for B002 (see Fig. 21). Also, as shown in Fig. 22, the vorticity budget Ω^+ generated in the tip region of the propeller is much lower for setting B002 and consequently the strength Γ of the vortices. So far, everything is as expected at first.

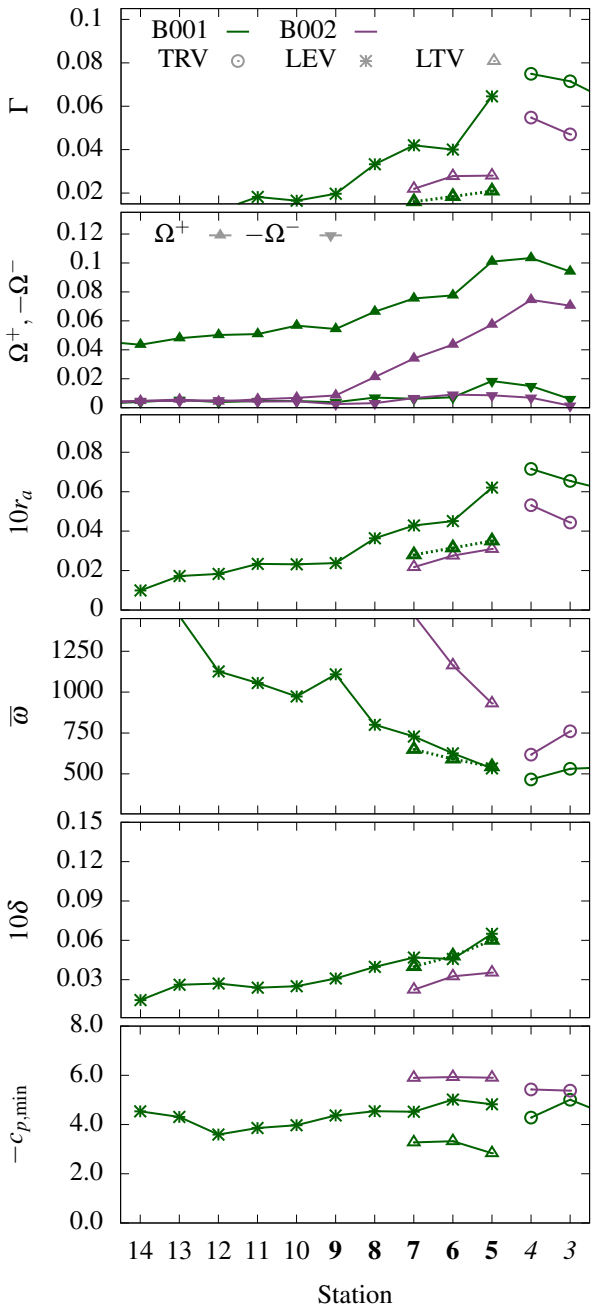

Figure 22: Vortex quantities for local tip vortex (LTV), leading edge vortex (LEV) as well as for the trailing vortex (TRV) evaluated at different extraction planes along the leading edge (planes 14 to 10), propeller tip (planes **9** to **5**) and downstream of the propeller tip (planes *4* and *3*). Setting B001 and B002. Dotted lines indicate that vortex quantities were evaluated manually.

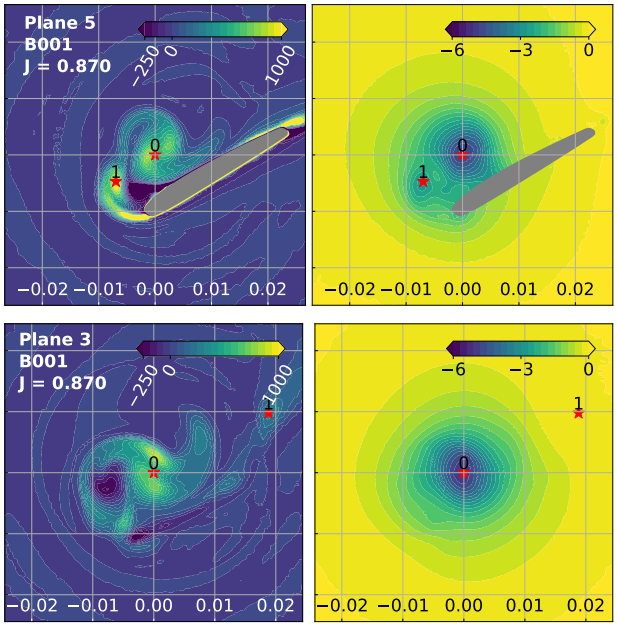

(a) Setting B001.

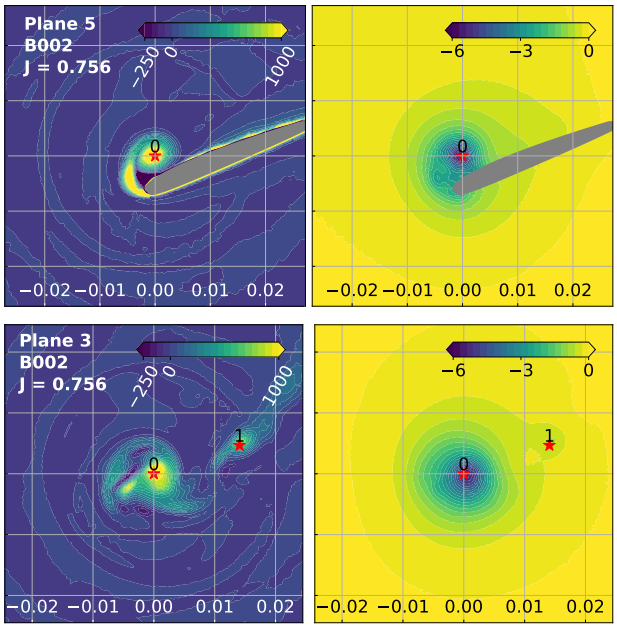

(b) Setting B002.

Figure 23: Distribution of vorticity ω_3 (left-hand side of the subfigures) and pressure coefficient c_p (right-hand side) for setting B001 and setting B002. Operation conditions as in Tab. 4. Plane 5 located at the blade tip; plane 3 downstream of the propeller tip. Red stars ⋆ mark locations of local pressure minima. See Section 3 for explanation.

The reason for the cavitation inception speed being lower despite a smaller vorticity budget available is to be sought again in the distribution of vorticity. In Fig. 23a, a dominant leading edge vortex with a co-existing local tip vortex can be clearly seen for setting B001 resulting in a category IV-trailing vortex. As discussed in the previous sections, this leads to low levels of vorticity $\overline{\omega}$ in the core of the vortex.

On the other side, as shown in Fig. 23b for setting B002, no leading edge vortex is generated and only a compact local tip vortex can be found exhibiting very high levels of vorticity (category I). The large difference in the vorticity level leads to a more intense pressure drop in the vortex core in the case of B002, even though the vortex circulation Γ is smaller.

Fig. 24 shows the cavitation patterns observed for setting B001 and setting B002 during the cavitation inception tests. The experimental results perfectly confirm the aforementioned. For setting B001, apart from the cavitating trailing vortex, a cavitating leading edge vortex can be clearly seen (for better visibility it has been highlighted by a green line), whereas for setting B002, only a local tip vortex transitioning into the trailing vortex is visible (violet line).

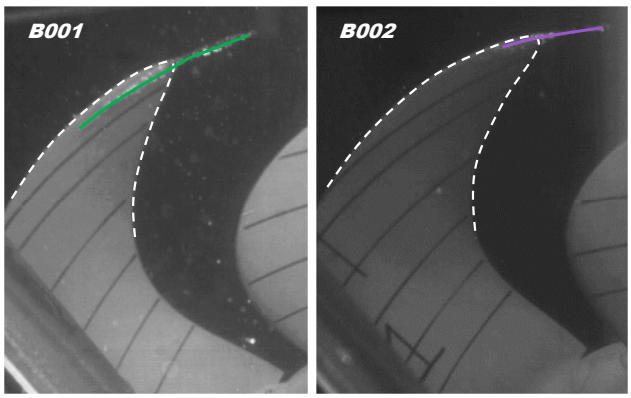

Figure 24: LTV/TRV cavitation for settings B001 (left-hand side of the figure) and B002 (right-hand side). Operation conditions as in Tab. 4 with reduced ambient pressure; i.e. cavitation well beyond inception for better visibility of the vortex structures.

6 CONCLUSIONS AND FUTURE WORK

Within this study, the behaviour of vortex structures at the propeller tip has been systematically investigated for a number of different flow configurations. In particular, the question has been addressed, in how far the local tip vortex and the leading edge vortex affect the structure of the trailing vortex. In the last section of this paper, we would like to sum up our findings, discuss the implications on the design of silent and efficient propellers and see which aspects should be addressed in future work.

6.1 Main Findings

The pressure drop in a vortex depends on both the strength of the vortex in terms of circulation Γ, i.e. the overall amount of vorticity accumulated in the vortex, and the levels of vorticity that are reached in the core or – in other words – the distribution of vorticity. Three possible mechanisms leading to reduced levels of vorticity in the core of the trailing vortex have been identified and discussed:

(i) Merging of local tip vortex and leading edge vortex,

(ii) entrainment of an increased amount of negative vorticity that is generated when the leading vortex forms along the leading edge, and,

(iii) suppression of the local tip vortex promoting the dominant leading edge vortex with relative high viscous core radius and low levels of vorticity to transition into the trailing vortex.

In the study, a large number of flow configurations was encountered that can be divided into four categories; for each of these categories one or more of the above effects could be observed leading to different levels of vorticity in the core of the trailing vortex.

In many cases, the inception of cavitation happens in the core of the trailing vortex; however, this is not always the case. Within the study, some configurations displayed cavitation inception in the leading edge vortex or the local tip vortex close to the blade tip.

Vortices were characterised mainly in terms of circulation, viscous core radius and the pressure drop in the vortex core. Here, a fitting procedure involving the Batchelor vortex model was applied in order to extract these quantities. It could be seen that, for trailing vortices downstream of the propeller tip, the fitting method delivers good results. However, for vortices close to the blade surface or during the merging process, it may become challenging to model the velocity profile by a Batchelor vortex.

6.2 Propeller Design Strategies

Tip unloading is a well-established strategy to reduce the pressure drop in the core of the trailing vortex and thus to increase cavitation inception speed. This method targets limiting the strength of the vortex structures in the tip region. It is effective, however, it is inherently tied to losses in propulsive efficiency. Alternative design strategies are based on locally manipulating the distribution of vorticity that it generated at the propeller tip. In particular, by applying tip rake to the propeller, it is possible to suppress the local tip vortex and accumulate free vorticity in a leading edge vortex with large core and consequently low levels of vorticity.

In general, the designer should strive to avoid blade tips that favour the formation of a “sharp” and compact local tip vortex, since in most cases this results in high vorticity levels and early cavitation onset. Tip rake has proven to be one effective mean to delay cavitation inception, however, alternative approaches involving blade thickness, profile type, the camber distribution and rounding the edges of the propeller tip should be taken into consideration as well. The framework for analysis developed in this paper will be of help when assessing these different approaches.

A good silent propeller design shows favourable characteristics for a wide range of operation conditions. However, it has been demonstrated that the behaviour of the vortex structures at the propeller tip strongly depends on the operation condition and – in case of controllable pitch propellers – on the pitch setting. A given strategy to delay cavitation inception might work well for one particular operation condition, it might fail for another. In other words, the larger the variation of inflow angle faced by the propeller, the more difficult it gets to find a design that features high cavitation inception speed without compromising on efficiency. It is therefore important to aim for a wake field being as homogeneous as possible. Thus, the aft ship has to be an integral part of the design process; especially when silent propulsion systems are concerned.

6.3 Future Work and Improvements

For the analysis, a RANS approach has been used to characterise vortex structures at the propeller tip. The flow patterns observed are quite complex and display many effects, such as separation, merging of co-rotating and contra-rotating vortices as well as boundary layer–vortex interaction. Even though, the shortcomings of the RANS approach are well-known when dealing with vortical flow, it is assumed that the approach still provides valuable insights into the behaviour of the propeller tip flow, albeit mainly in a qualitative manner. Future work should therefore address applying scale-resolving methods such as LES or DES.

Also within future work, more robust methods for vortex characterisation should be tested. For instance, with Eqs. (9), (11) and (12), it is theoretically possible to retrieve Γ and r_a by evaluating $c_{p,\min}$ and $\omega_{\psi,\max}$ in the center of the vortex. Still, the characterisation would be based on the Batchelor vortex model; however, the need for data fitting would be eliminated.

Furthermore, a more advanced analysis of leading edge vortex and local tip vortex as shown by Wojcik and Buchholz (2014) or Eldredge and Jones (2019) for a leading edge vortex configuration should be considered. With their problem-adapted control volume analysis, it could be possible to gain further insights into vorticity generation and transport.

Another important aspect that should be covered by future research is the investigation of scale effects with respect to the Reynolds number. So far, when conducting cavitation inception experiments, the results for vortex cavitation are scaled by McCormick's method (described in the ITTC guidelines, NN 2017), disregarding the nature and the origin of the vortex. In particular, it should be addressed in how far this simple scaling approach is adequate for the complex vortex structures at the propeller tip.

ACKNOWLEDGEMENTS

The authors would like to thank Dr.-Ing. Dag Feder, former Hamburg University of Technology, for his valuable suggestions.

For the competent and informative discussion of the cavitation test results presented in Section 5, we would like to thank the Propeller and Cavitation Team of the Maritime Research Institute Netherlands (MARIN).

NOMENCLATURE

Propeller flow	
R, $D = 2R$	Propeller radius, diameter
n, V	Number of revolutions, inflow speed
V_{inc}	Vortex cavitation inception speed
ρ	Density of water
$J = {}^{V}/_{nD}$	Advance ratio
$k_T = {}^{T}/_{\rho n^2 D^4}$	Thrust coeff. with thrust T
$k_Q = {}^{Q}/_{\rho n^2 D^5}$	Torque coeff. with torque Q
$\eta = {}^{J}/_{2\pi}{}^{k_T}/_{k_Q}$	Efficiency
$k_{T,r}$	$= {}^{\mathrm{d}T}/_{\rho n^2 \mathrm{d}r D^3}$, sectional thrust coefficient
${}^{P}/_{D}$	Pitch ratio
${}^{x_{\text{tip}}}/_{R}$	Tip rake
Flow quantities	
$\mathbf{x}' = (x', y', z')$	(Dimensional) position vector in Cartesian coordinates
$\mathbf{v}'$, $\boldsymbol{\omega}' = \nabla \times \mathbf{v}'$	(Dimensional) flow velocity and vorticity
$\mathbf{x} = (x, y, z)$	$= {}^{1}/_{D}\mathbf{x}'$, non-dimensional position vector in Cartesian coordinates
$\mathbf{v}$	$= {}^{1}/_{nD}\mathbf{v}'$, non-dim. flow velocity
$\boldsymbol{\omega}$	$= {}^{1}/_{n}\boldsymbol{\omega}'$, non-dim. vorticity
$c_p = \frac{p - p_{\text{ref}}}{\rho n^2 D^2}$	Pressure coefficient
Vortex analysis	
Γ, r_a	Vortex circulation and viscous core radius
$c_{p,\min}$	Pressure drop in the vortex core
δ	Wall distance
ω_3	Vorticity component normal to extraction plane
Ω^+, Ω^-	Positive and negative vorticity budget (see Section 2.4)
$\overline{\omega}$	$= {}^{\Gamma}/_{\pi r_a^2}$, averaged vorticity level in the vortex core
t_1, t_2, t_3	Local coos. in the extraction plane with basis vectors $\mathbf{t}_1$, $\mathbf{t}_2$, $\mathbf{t}_3$ (surface normal)
ξ, φ, ψ	Cylindrical vortex coos. with basis vectors $\boldsymbol{\xi}$, $\boldsymbol{\varphi}$, $\boldsymbol{\psi} \parallel \mathbf{t}_3$ (pointing along the vortex axis)

REFERENCES

(The list of references continues on the page after next.)

Amini, A., Reclari, M., Sano, T., Iino, M., and Farhat, M. (2019). Suppressing tip vortex cavitation by winglets. Experiments in Fluids, 60(159).

Asnaghi, A., Svennberg, U., and Bensow, R. E. (2018). Numerical and experimental analysis of cavitation inception behaviour for high-skewed low-noise propellers. Applied Ocean Research, 79.

Asnaghi, A., Svennberg, U., and Bensow, R. E. (2019). Evaluation of curvature correction methods for tip vortex prediction in SST k-omega turbulence model framework. International Journal of Heat and Fluid Flow, 75:135–152.

Asnaghi, A., Svennberg, U., Gustafsson, R., and Bensow, R. E. (2021). Propeller tip vortex mitigation by roughness application. Applied Ocean Research, 106.

Brown, M., Schroeder, S., and Balaras, E. (2015). Vortex structure characterization of tip-loaded propellers. In Fourth International Symposium on Marine Propulsors, Austin, Texas, USA.

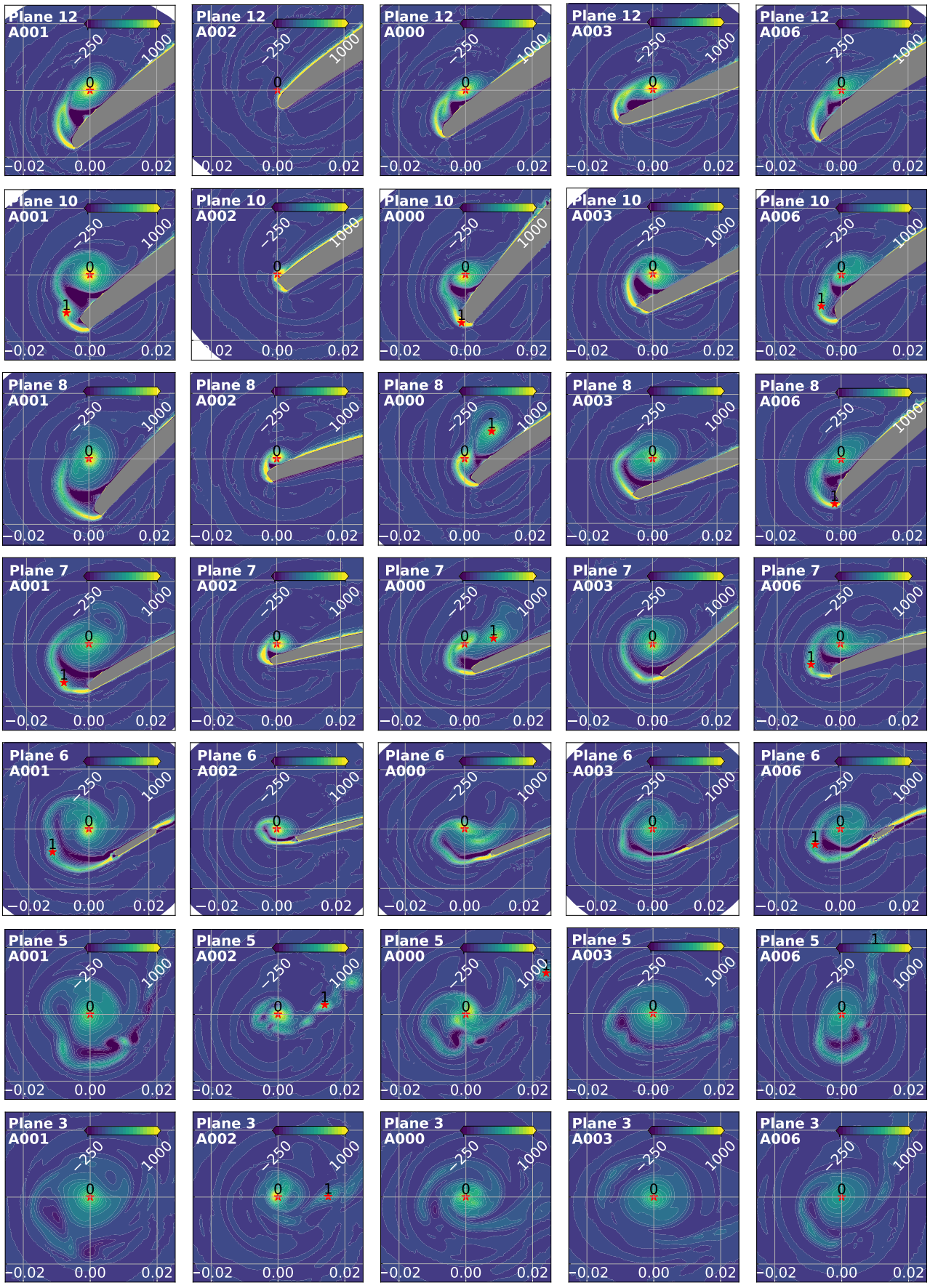

(a) Variant A001. **(b)** Variant A002. **(c)** Baseline prop. A000. **(d)** Variant A003. **(e)** Variant A006.

Figure 25: Distribution of vorticity ω_3 for baseline propeller A000 and variants A001, A002, A003 as well as A006 at different stations along leading edge (plane 12), propeller tip (planes 10, 8, 7 and 6) and downstream of the tip (planes 5 and 3) at $J = 0.85$.

Devenport, W. J., Rife, M. C., Liapsis, S. I., and J., F. G. (1996). The structure and development of a wing-tip vortex. J. Fluid Mech., 312:67–106.

Eldredge, J. D. and Jones, A. R. (2019). Leading-edge vortices: Mechanics and modeling. Annu. Rev. Fluid Mech., 51:75–104.

Feder, D. F. (2021). Evolution of trailing vortices around a ship hull at large drift angle. Dissertation, Hamburg University of Technology, Hamburg.

Isay, W. H. (1991). Eine Näherungslösung für das Geschwindigkeits- und Druckfeld eines Flügelspitzenwirbels in turbulenter Strömung. Technical Report 516, Institut für Schiffbau der Universität Hamburg, Hamburg, Germany.

Kissing, J., Kriegseis, J., Li, Z., Feng, L., Hussong, J., and Tropea, C. (2020). Insights into leading edge vortex formation and detachment. Experiments in Fluids, 61(208).

Krüger, C. (2017). Hydrodynamische Wirkung von Flügelspitzenrauigkeiten an Schiffspropellern auf den Spitzenwirbel und die Spitzenwirbelkavitation. Dissertation, University of Rostock, Rostock.

Kuiper, G. (2001). New developments around sheet and tip vortex cavitation on ships' propellers. In Fourth International Symposium on Cavitation, Pasadena, California, USA.

Langtry, R. and Menter, F. (2009). Correlation-based transition modeling for unstructured parallelized computational fluid dynamics codes. AIAA Journal, 47(12):2894—2906.

Li, Z., Feng, L., Kissing, J., Tropea, C., and Wang, J. (2020). Experimental investigation on the leading-edge vortex formation and detachment mechanism of a pitching and plunging plate. J. Fluid Mech., 901.

Menter, F. R. (1994). Two-equation eddy-viscosity turbulence models for engineering applications. AIAA Journal, 32(8):1598–1605.

Meunier, P., Le Dizes, S., and Leweke, T. (2005). Physics of vortex merging. C. R. Physique, 6:431–450.

NN (2017). 7.5-02-01-05 Model-Scale Propeller Cavitation Noise Measurements. Technical report, ITTC.

NN (2022). Siemens Simcenter STAR-CCM+ Documentation Version 2206. Technical report, Siemens Digital Industries Software, Plano, Texas, USA.

Park, I., Kim, J., Paik, B., and Seol, H. (2021). Numerical study on tip vortex cavitation inception on a foil. Applied Sciences, 11.

Paskin, L., Visonneau, M., Guilmineau, E., and Wackers, J. (2019). Computational modeling of turbulent flows on the tip vortex of a marine propeller's blade. In Sixth International Symposium on Marine Propulsors, Rome, Italy.

Peric, M. (2022). Prediction of tip vortex flows on propeller blades using adaptive grid refinement. In 24th Numerical Towing Tank Symposium, Zagreb, Croatia.

Widmann, A. and Tropea, C. (2015). Parameters influencing vortex growth and detachment on unsteady aerodynamic profiles. J. Fluid Mech., 773:432–459.

Wojcik, C. J. and Buchholz, J. H. J. (2014). Vorticity transport in the leading-edge vortex on a rotating blade. J. Fluid Mech., 743:249–261.